DUAL POLARIZATION RADAR LAGRANGIAN PARAMETERS: A STATISTICS-BASED PROBABILISTIC NOWCASTING MODEL

Bruno L. Medina and Luiz A. T. Machado

Centro de Previsão de Tempo e Estudos Climáticos, Instituto Nacional de Pesquisas Espaciais, Cachoeira Paulista, Brazil

Submitted to Natural Hazards

September 2016

Corresponding Author: Bruno Lisbôa Medina, email: bmedina@nsstc.uah.edu, +1 2568244031

Present Address: Department of Atmospheric Science, University of Alabama in Huntsville, 320 Sparkman Dr, NW, Huntsville, AL, 35805 USA

Acknowledgments

We would like to thank the CHUVA project, supported by Fundação de Amparo à Pesquisa do Estado de São Paulo (FAPESP), Grant 2009/15235-8 and 2015/14497-0. The first author was financed by CNPq, process 132660/2013-0 during his Master's degree and by CNPq project, process 400043/2014-9.

Abstract

The aim of this study is to present a statistics-based Lagrangian nowcasting model to predict intense convective events based on dual polarization radar parameters. The data employed in this study are from X-Band radar collected during the CHUVA-Vale campaign from November 2011 to March 2012 in southeast Brazil. The model was designed to catch the important physical characteristics of storms, such as the presence of supercooled water above 0 °C isotherm, vertical ice crystals in high levels, graupel development in the mixed phase layer, and storm vertical growth, using polarimetric radar in the mixed-phase layer. These parameters are based on different polarimetric radar quantities in the mixed phase, such as negative differential reflectivity (Z_{DR}) and specific differential phase (K_{DP}), low correlation coefficient (ρ_{hv}) and high reflectivity Z_h values. Storms were tracked to allow the Lagrangian temporal derivation. The model is based on the estimation of the proportion of radar echo volume in the mixed phase that is likely to be associated with intense storm hydrometeors. Thirteen parameters are used in this probabilistic nowcasting model, which is able to predict the potential for future storm development. The model distinguishes two different categories of storms, intense and non-intense rain cell events by determining how many parameters reach the "intense" storm threshold.

Keywords: Nowcasting, Dual polarization radar, Microphysics, CHUVA Project.

1 Introduction

Dual polarization radar provides very useful information for short-term forecasting (nowcasting) because it offers information that allows for the inference of cloud microphysical properties as a result of the differences and/or similarities in the signals from the horizontally and vertically polarized channels. Some additional variables afforded by this radar compared to single polarization radar are differential reflectivity (Z_{DR}), differential phase (Φ_{DP}), specific differential phase (K_{DP}) and correlation coefficient (ρ_{hv}) (for definitions of variables, see Kumjian 2013). Due to the sensitivities of these variables to hydrometeor type, size, shape, and concentration, polarimetric radar information can be used to interpret cloud microphysical properties and physical processes. Although nowcasting techniques based on meteorological radar data have been developed in the past few decades, the use of dual polarization radar data in nowcasting applications is still relatively unexplored. Studies in this area are primarily based on dual polarization microphysical interpretations, which are signatures for severe event case studies or their relationship with lightning. This study explores the time evolution and trend of storm dual polarization variables as a proxy of intense convection.

Some authors have evaluated the backscattering properties of polarimetric observations for different hydrometeors, such as Aydin *et al.* (1984), Aydin and Seliga (1984) and Matrosov (1996). In addition, an important improvement is the hydrometeor classification development, which has been widely performed using the fuzzy logic method (Vivekanandan *et al.* 1999; Al-Sakka *et al.* 2013) and simulations using the scattering model (Straka 2000; Dolan and Rutledge 2009). Several studies have used polarimetric variables to describe the physical processes of specific meteorological events. For example, Dotzek and Friedrich (2009) used hydrometeor classification with dual polarization radar and observed that melting hydrometeors and the evaporation of liquid water and large hail drag are the main contributing factors to the occurrence of downbursts. For severe thunderstorms, polarimetric signatures of supercells were studied by Kumjian and Ryzhkov (2008). They found that high Z_{DR} arc, which is caused by storm-relative winds, Z_{DR} and K_{DP} columns associated with updrafts, depressed ρ_{hv} holes, which are caused by mixed-phase and resonance-sized hydrometeors, and high Z_{DR} rings, which are caused by water-coated ice particles, increasingly oblate. Evaristo *et al.* (2013) showed that small conical graupels with small apex angles are associated with a Z_{DR} less than 0 dB. In general, considering the range of apex angles, the mean Z_{DR} signature is negative and Z_h is relatively high. Very large and irregularly shaped hail also has a negative Z_{DR} feature (Straka *et al.* 2000). Otherwise, for melting hail, Z_{DR} can be significantly higher than 0 dB (Ryzhkov *et al.*, 2013a, b).

Polarimetric variables have been widely used for storm electrification studies. Evidence for the vertical alignment of ice crystals at upper levels of thunderstorms due to strong electric fields have been documented by Hendry and McCormick (1976), Weinheimer and Few (1987) and Foster and Hallet (2002). These are important conditions for cloud electrification because for polarimetric variables, they lead to negative Z_{DR} values in the glaciated phase region (Ryzhkov and Zrnic, 2007; Dolan and Rutledge, 2009). Jameson (1996) verified the appearance of a significant volume of positive Z_{DR} at -7 ºC, corresponding to the process of large liquid raindrops and subsequent freezing as a proxy of the onset of electrification. Woodard *et al.* (2012) verified a graupel at -15 ºC and Z_{DR} column (Z_{DR}> 1 dB) at -10 °C as predictors of lightning. Van Lier-Walqui *et al.* (2015) observed a K_{DP} column feature, which consists of a positive K_{DP} above the melting layer that is associated with updrafts, lightning and intense rainfall. Lund (2009) also verified a Z_{DR} column above 0 ºC isotherm (3-6 km above mean sea level), suggesting that graupel formation in this region is an important feature for lightning initiation. Using a large number of events observed by X-band radar, Mattos *et al.* (2016a) found positive Z_{DR} above -15 ºC isotherm for high lightning frequency, as well as Z_h up to 45 dBZ and K_{DP} around +1 º km^{-1} between 0 ºC and -15 ºC isotherm, which was associated with raindrops carried by strong updrafts. In the glaciated phase layer, above -30 ºC isotherm, authors have found enhanced negative K_{DP} values of -0.5 º km^{-1} for high lightning frequency.

Lagrangian tracking for radar echo studies is widely used along with nowcasting techniques (Bellon *et al.* 2010; Morel *et al.* 1997; Johnson *et al.* 1998; Dixon and Wiener 1993; Lakshmanan and Smith 2010). Additional research about rain cell clusters tracking for physical interpretation has been done for graupel volume and dual polarization properties associated with lightning (Carey and Rutledge 1996, 2000) and graupel mass (Deierling et al. 2008; Deierling and Petersen 2008). Our study also focuses on storms from a Lagrangian perspective, as an automated tracking algorithm is used to identify and track a rain cell.

The abovementioned studies demonstrate the important capability of dual polarization radar to observe storm features and describe their degree of severity. The additional information provided by dual polarization radar compared with single polarization radar shows a strong potential to improve nowcasting techniques and lead-time in nowcasting models. The main objectives of this study are to a) evaluate and quantify the predictability of nowcasting parameters using dual polarization radar data and b) propose a statistical model for nowcasting intense convective events based on Lagrangian tracking of convective cells.

Section 2 presents the data and methodology used in this study, Section 3 presents the dual polarization radar Lagrangian parameter calculation, and its evaluation is shown in Section 4. Section 5 describes the nowcasting model, and conclusions are provided in Section 6.

2 Data

The data used in this study are from the CHUVA Project (“rain” in Portuguese, acronym for Cloud Processes of the Main Precipitation Systems in Brazil: A Contribution to Cloud-Resolving Modeling and to the Global Precipitation Measurement (GPM)), which consists of field experiments that evaluate cloud processes of the different precipitation regimes in Brazil (Machado *et al.* 2014). This study uses data collected during the CHUVA-Vale campaign, which has significant potential for the development of nowcasting tools due to the availability of good quality, high time-space resolution of a 9.375 GHz X-Band dual polarization radar (DX50 Selex) data for several intense convective events. In this campaign, the radar was installed in Sao Jose dos Campos (23º12’ S, 45.54’ W) from November 1, 2011 to March 31, 2012 (Figure 1).

The X-Band radar data were pre-processed for precipitation attenuation in reflectivity and differential reflectivity. For the reflectivity attenuation correction, ZPHI algorithm was used (Testud *et al.* 2000; Schneebeli *et al.* 2012). Precipitation over radar occurred only 3 times for the selected events (0.007% of cases). For these cases, a correction proposed by Bechini *et al.* (2010) was applied. For the Z_{DR} correction, the linear Φ_{DP} method that considers Z_{DR} attenuation to be linearly proportional to Φ_{DP} (Bringi 2007) was employed. Z_{DR} offset was removed based on the vertical pointing strategy before each volume scan (Sakuragi and Biscaro 2012). A detailed description of the corrections employed is detailed in Machado *et al.* (2014), Mattos *et al.* (2016a) and Schneebeli *et al*. (2012). Possible resonance effects caused by interference from electromagnetic waves reflected by the edges of the drops and cross-coupling between the orthogonally polarized waves (Ryzhkov and Zrnic 2005) or non-filling beans effects were not considered in the corrections. The radar strategy employed during the campaign was composed of 13 elevations every 6 minutes, with angular and radial resolutions of 1 ° and 150 m, respectively, one RHI and 1 vertical pointing. The maximum range was 100 km (Machado *et al.* 2014), but in this study, a maximum range of 60 km was used to avoid larger attenuation at a high distance from the radar.

3 The Lagrangian Calculations and Vertical Profiles

The basic hypothesis for the statistics-based probabilistic nowcasting model development was that the dual polarization parameters and trends are able to capture information about storm intensity during the storm's life cycle before the storm becomes "intense" (the definition for intense storms in this work is provided in Section 4b). A tracking algorithm was employed to follow the rain cells and for the calculation of the Lagrangian parameters and its time derivation. The tracking algorithm employed was the ForTraCC (Forecast and Tracking the Evolution of Cloud Clusters; Vila *et al.* 2008). Tracking was performed using 3 km CAPPI, followed by 35 dBZ reflectivity structures (hereafter called rain cells) and using the threshold of an area of 0.2 km^2 overlap between consecutive scans (for the 6-minute interval). In cases of a rain cells split, the cell's life cycle that was chosen for continued tracking was the cell with a higher maximum reflectivity. Originally, ForTraCC was designed to continue tracking with the largest cell in the split cell's cases; however, our study verified that following the core of maximum reflectivity is more appropriate for nowcasting (not shown). For each rain cell, a 3-D grid with 1 km horizontal and 0.5 km vertical resolutions were built based on the volume scan. For each 1x1x0.5 km box, a bin value was chosen from the bin population inside the box, depending on the physical characteristics, such as the minimum and maximum polarimetric variable value. If a box does not contain any radar bin, then the box is filled with a value linearly interpolated by the closer vertical neighbors, constituting all vertical profiles.

After the 3-D data rearrangement, layers of interest for obtaining dual polarization intense convective events potential characteristics were defined. Layers were defined between the isotherms that were obtained from an average reference radiosonde released during the campaign. The layer of interest was the mixed-phase Layer (MPL), defined between 0 ºC and -40 ºC isotherms. Two mixed-phase sub-layers were defined in this study, mixed-phase layer 1 between 0 °C and -15 °C (MPL-1) and mixed-phase layer 2 (MPL-2) between -15 °C and -40 °C. Mattos *et al.* (2016a) also utilized these sub-layers.

4 Nowcasting parameters calculations

a General calculations

Potential nowcasting parameters were acquired after obtaining the 3-D grid data for each rain cell. Storm sub-volumes of specific characteristics defined by the polarimetric variables were computed for the MPL layer and sub-layers. This was translated to the cells defined by the area of 35 dBZ at 3 km every 6 minutes, which makes Lagrangian calculations possible. The set of parameters, as well the expected values, are consistent with the physical interest of the studied layer for intense convection, based on the characteristics of the dual polarization intense convective events.

A typical storm life cycle, from the beginning to its maturation phase, presents the following features: low level convergence, vertical growth, formation of ice crystals in high levels, updrafts carrying liquid water to levels above 0 °C isotherm in supercooled water, and graupel formation in mixed phase layer by the riming process. These physical processes before the maturation phase were analyzed through the representative parameters measured by radar variables. The computed parameters are:

a) Echo top time variation as a proxy of the cloud vertical velocity;
b) Vertically Integrated Liquid (VIL) to estimate the total mass of precipitation (Greene and Clark 1972);
c) Reflectivity $Z_h \geq 35$ dBZ between 0 ºC and -40 °C isotherms (MPL) to estimate the number and, mainly, the size of hydrometeors;
d) $K_{DP} \geq 0$ ° km^{-1} between 0 ºC and -15 ºC (MPL-1) to describe regions with updrafts (supercooled liquid water) above the melting layer (van Lier-Walqui *et al.* 2015);
e) $K_{DP} < 0$ ° km^{-1} in MPL-2, between -15 ºC and -40 ºC isotherms, to describe regions with ice crystal formed above the updraft of the supercooled liquid water (Mattos *et al.* 2016b);
f) $Z_{dr} < 0$ dB between 0 ºC and -40 ºC (MPL), implying a vertically oriented ice crystals content in this layer (Aydin and Seliga 1984);
g) $\rho_{hv} \leq 0.9$ between 0 ºC and -15 ºC (MPL-1), implying the presence of hydrometeors in different phases in the same sample volume (Tuttle *et al.* 1989).

The 1x1x0.5 km storm pixels were filled by a maximum polarimetric variable value for parameters a-d and with minimum values for parameters e-g. This is an important procedure because sometimes, the variable needs to be higher, such as the reflectivity or VIL, or smaller, such as Z_{DR}, to describe graupel in the mixed phase.

The storm process toward the convective intense stage can be described by the volume fraction of the parameters described above or by the trend of these volumes. The hypothesis is that the mixed phase region is filled with these representative parameters measured by radar variables as the ordinary cloud moves to a thunderstorm with intense characteristics (reaches the 60 dBZ reflectivity). Therefore, after the set of parameters were determined, the volume fraction (compared to the total volume of MPL) and the Lagrangian temporal derivatives (the trends) of these volumes were performed. These volume fractions and trends are considered as potential estimators of nowcasting.

b The selection of intense and non-intense convective events.

To test the parameters shown in the last section, intense events were defined in this study as any rain cells reaching at least 60 dBZ at 3 km height, any time during the life cycle. Non-intense events were defined as rain cells that did not meet the above criteria, but that had at least one pixel with reflectivity between 45 and 55 dBZ at 3 km height during its life cycle. We added this additional criterion for non-intense events to have a strong control dataset, thus avoiding ordinary storms. For the intense events definition, it is assumed that a significant amount of large drops and/or hail is present in a storm's low level (below freezing level). It is also assumed that this precipitation/hail amount would affect the surface by intense rainfall or hail by continuity and/or downbursts by precipitation drag or hail melting. For the non-intense events definition, it is assumed that the storm has limited intense features because in most of the storm's area coverage and life cycle, the Z_h values are much lower than 55 dBZ. It is also assumed that non-intense events have a small probability of having hail or downbursts due to the limited imposed condition, and at the same time, they avoid ordinary storms that are easily identified by our criterion. For intense events, it is necessary to define "event time", which is the time of the occurrence of 60 dBZ. This definition is very important for the verification of the lead time to nowcast the events.

Twenty-nine intense and nineteen non-intense events were obtained, and all parameters were calculated. From the twenty-nine intense events, the last 10 were used to evaluate the model and are defined as independent cases. No non-intense events were tested in this evaluation. Each case was carefully analyzed visually, and no significant signal extinction happened on any case, likely due to the 60 km radius limit and because these cells were not interfered by other convective cells (isolated cells). Cases where some extinction was clearly present were not considered in this study. Figure 1 shows the selected events location at its maximum reflectivity time, and Figure 2 shows the maximum reflectivity time evolution of all events.

c Adjustments of parameters threshold and application to events

For each event's time step, the volume fraction of representative parameters measured by radar (volume % of the total MPL volume) and the Lagrangian volume temporal derivative (the trend of the volume fraction) were computed. For intense events, the time of the occurrence of the maximum value (the volume fraction or trend of the specific parameter) before the event time (when the rain cell reached 60 dBZ for the first time) was saved. This procedure was followed to study the lead time of each computed parameter. Figure 3 shows the frequency of occurrence of the lead time, i.e., the time when the maximum value of each parameter was reached before the "event time". This result shows that the volume fraction and the trends of the selected parameters can predict the intense convective event before it reaches the "event time". It is important to highlight that VIL and its trend and echo top time variations were the only parameters for which the volume fraction was not computed. The maximum frequency of these maximum values occurs 6 minutes before the event time, while the average and median time is 14.7 and 12 minutes, respectively.

The different lead time of each parameter is clear. The largest lead time was observed for parameter 10 (see Table 1), Z_{DR}<0 relative volume in the MPL, parameter 11, and echo top time variation. The likely reason for the larger echo top time variation lead time is that these parameters roughly describe the intensity of the cloud vertical motions during the growing phase, before the system reaches the maximum cloud top height. The Z_{DR}<0 relative volume describes the increase of the vertical ice crystals and graupel content and is also a good parameter with a large lead time, which is a feature that precludes the first lighting occurrence (Mattos *et al.* 2016b). Interestingly, the relative volume of positive K_{DP} in MPL-1 (parameter 4 in table 1), a parameter related to updraft stretching, shows a peak 30 minutes before the event time, resulting in an important contributor for increasing lead time for intense convective events.

The result presented in Figure 3 shows a coherent increase as the lead time decreases. However, it should be noted that the maximum volume fraction or trend can occur in different lead times. Therefore, to design a statistics-based model for nowcasting, we should consider a probability perspective, as the set of parameters has two main characteristics: a) an increase in probability detection as the event time gets closer and b) the maximum volume fraction or trend can have the maximum value at different time intervals before the event time. To obtain a probabilistic model, we should consider the probability for all parameters (volumes fraction, trends and echo top rate) to indicate the occurrence of intense convective events. We expect to have an increase in probability as the time moves closer to the intense weather event time.

We have defined a specific threshold for each parameter to build the probability model. For the parameter threshold value definition (volume fraction, trends or echo top rate), the threshold value must be reached during the 12-minute lead time for an intense event forecast. The use of 12 minutes for the calculation will be discussed in the next section. If the parameter threshold is not reached for an event in this lead time window, then it does not forecast an intense event. We then applied a modified contingency table (Table 2) where just “hits” and “misses” are possible (no false alarms and correct negatives). For an intense event, if the parameter threshold is reached at or before 12-minute lead time, it is “hit”, and if it is not reached, it is a “miss”. For non-intense events, “hit” and “miss” definitions are the opposite, but the entire event’s life cycle is analyzed. Considering this strategy, we were able to calculate the probability of detection, while other statistics such as the false alarm ratio could not be calculated. This was applied to obtain a single evaluator that encompasses both intense and non-intense events. Then, a threshold adjustment was performed by testing different values to obtain the best threshold with the maximum POD. For echo top rate, in addition to the threshold, it was also necessary to test the reflectivity Z_h of the cloud top. Cloud top was defined by the 40 dBZ reflectivity threshold because it provided the best POD score. In this manner, 13 parameters were defined, as presented in Table 1.

5 The Statistics-Based Probabilistic Model

Based on the parameters shown in Section 4.3 (Table 1), a statistics-based probabilistic model that integrates all parameters was developed, which allows for the determination of whether along the cell life cycle evolution the rain cell will evolve into an intense event. Applying the 13 parameters to an intense event, it was determined how many parameters reached its threshold for each time step. The probability is computed if the threshold is reached in the last two time steps (12 minutes). This twelve-minute accumulation, as defined in the last section, is due to the difficulty of considering only one time step because of the great event's and parameters' lead time variability. The number of parameters that provided an alert results in a percentage probability of occurrence of an intense event. An average of the probability for all nineteen intense events and its standard deviation in terms of the lead time is shown in Figure 4. For comparison, the probability average and standard deviation without accumulating the last time steps, as well as accumulating only the time step before it (6 minutes accumulated), are also shown. It can be seen that the probability increases as the time accumulated gets higher. With accumulating 12 minutes, the probability increases continually as the event time approaches. Generally, approximately 70% of the parameters indicated an intense event alert in 24- to 12-minute lead time, and approximately 80% indicated an intense event alert in 6-minute lead time. Six and zero minutes accumulated have lower probabilities, and some steps have decreasing probability with decreasing lead time, which is not an expected or reliable performance, thus justifying the use of the 12-minute accumulation in time. Lead times higher than 30 minutes were neglected in this analysis because of the large uncertainties and noise that occurs with large lead time values not associated with the intensity of the event.

Applying the set of parameters to the independent events (blue line in Figure 5), a similar behavior compared to the original set of intense events (black line in Figure 5) can be seen, with increasing probability with decreasing lead time, except from -18- to -12-minute lead time, where a slight decrease of approximately 0.2% is verified. Analyzing each independent event individually (yellow lines in Figure 5), it is seen that, for most cases, the probability remains high and inside the intense standard deviation area. From the ten independent events, four present a probability below the intense events standard deviation bar at least one time. On the other hand, nine of ten events present high probabilities inside the intense event standard deviation area in 6-minute lead time, and all events present probability inside this area at least once during their life cycle.

Figure 6 shows the probabilities for the nineteen non-intense entire life cycles, with the last event's time step plotted at 0 minutes on the x-axis. It can be seen that for ten of the nineteen non-intense events, the probability reaches values of 38-46% at least once, which is in the intense event 30-minute lead time standard deviation bar. For eighteen of the nineteen events, the probability does not reach 50%, which is above the intense event standard deviation bars for lead times lower than 24 minutes. One single non-intense event presents a very high probability during its life cycle and an intense event feature. This specific event was associated with a cell that merged with a second rain cell that evolved into an intense event, but at the same time, this second rain cell split, turning the tracking of the first rain cell to an erroneous life cycle. Because this event has a short life cycle due to this error and has a maximum reflectivity of 50 dBZ in 3 km cappi, it was characterized as a non-intense event in our study. Our criteria for non-intense events is very strong because the cell should not reach a value larger than 60 dBZ; however, it should reach values between 45 and 55 dBZ at least once. Therefore, this cell is not an ordinary rain cell, but it cannot be classified as an intense event because it did not reach the 60 dBz value during the life cycle.

While tracking a rain cell, the statistics-based probabilistic model correctly detects its future intensity. For an individual, independent intense event, the probability generally remained at 60% or higher, while for non-intense events, the probability did not reach 50%, except for one event. If applied operationally, this probabilistic model can help radar forecasters rank which rain cells should be followed as candidates for an intense convective event.

6 Conclusions

This work presents a probabilistic statistics-based nowcasting model that selects potential rain cells to become a cell with intense convection (≥60 dBZ). Because of the high reflectivity values of the non-intense events sample (rain cells reaching 45-55 dBZ) compared to intense events (≥60 dBZ), this is considered a very rigid model because it separates both types of storms. The model uses a set of thirteen parameters based on volume accounting of polarimetric variables. The physical meanings of these volume fractions or trends are consistent with well-known physical characteristics that are observed as storms develop, such as height top rate increases, increases of supercooled water above 0 °C isotherm, vertically aligned ice crystals and formation of graupel in the mixed-phase layer (Aydin and Seliga 1984; Tuttle *et al.* 1989; Bruning *et* *al.* 2007; Mattos *et al.* 2016a). Each parameter has its own capability to detect an earlier event with intense feature potential. Supercooled water immediately above 0 ºC isotherm, cloud top rate increases and vertical ice crystals content increases demonstrated the parameters with higher lead times. The relative volume occupied by these regions in the mixed phase layer or the trend of these volumes and the echo top rate captured the signature of the intensification process of these intense convective events. The definition of thresholds values for each parameter and the probability of reaching this threshold value in the last 12 minutes have been shown to be suitable for the probabilistic model.

An independent intense set of events was applied for testing and it performed well, which is consistent with the original set of intense events. The non-intense set of events was well separated from the intense and independent events, as most non-intense events have a higher probability than the intense event standard deviation area.

This study proposes 13 parameters based on the absolute value, relative volume and/or trends for nowcasting intense convective events. A sensitivity analysis of each parameter is presented, and a threshold is defined. Based on the 13 parameters and the threshold values, an operational model is proposed to select potential rain cells to become intense convective events. Its application in a large sample of events should be tested to present a quantitative evaluation of the methodology.

References

Al-Sakka H, Boumahmoud AA, Fradon B, Frasier SJ, Tabary P (2013) A new fuzzy logic hydrometeor classification scheme applied to the french X-, C-, and S-band polarimetric radars. J. Appl. Meteor. Climatol., 52:2328–2344. doi: http://dx.doi.org/10.1175/JAMC-D-12-0236.1

Aydin K, Seliga TA (1984) Radar polarimetric backscattering properties of conical graupel. J. Atmos. Sci., 41:1887–1892. doi: http://dx.doi.org/10.1175/1520-0469(1984)041<1887:RPBPOC>2.0.CO;2

Aydin K, Seliga TA, Bringi VN (1984) Differential radar scattering properties of model hail and mixed-phase hydrometeors. Radio Sci., 19:58-66. doi: 10.1029/RS019i001p00058

Bechini R, Chandrasekar V, Cremonini R, Lim S (2010) Radome attenuation at X-band radar operations. Proc. Sixth European Conf. on Radar in Meteorology and Hydrology, Sibiu, Romania, ERAD 2010, P15.1.

Bellon A, Zawadzki I, Kilambi A, Lee HC, Lee YH, Lee G (2010) McGill algorithm for precipitation nowcasting by lagrangian extrapolation (MAPLE) applied to the south korean radar network. Part I: Sensitivity studies of the Variational Echo Tracking (VET) technique. Asia-Pac. J. Atmos. Sci., 46:369-381. doi: 10.1007/s13143-010-1008-x

Bringi VN, Thurai M, Hannesen R (2007) Dual-polarization weather radar handbook. Selex-SI gematronik, 2nd edition, 163 pp.

Bruning EC, Rust WD, Schuur TJ, MacGorman DR, Krehbiel PR, Rison W (2007) Electrical and polarimetric radar observations of a multicell storm in TELEX. Mon. Wea. Rev., 135:2525-2544. doi: http://dx.doi.org/10.1175/MWR3421.1

Carey LD, Rutledge SA (1996) A multiparameter radar case study of the microphysical and kinematic evolution of a lightning producing storm. Meteor. Atmos. Phys., 59:33-64. doi: 10.1007/BF01032000

Carey LD, Rutledge SA (2000) The relationship between precipitation and lightning in tropical island convection: A C-band polarimetric radar study. Mon. Wea. Rev., 128:2687-2710. doi:http://dx.doi.org/10.1175/1520-0493(2000)128<2687:TRBPAL>2.0.CO;2

Deierling W, Petersen WA (2008) Total lightning activity as an indicator of updraft characteristics. J. Geophys. Res., 113:D16210. doi: 10.1029/2007JD009598

Deierling W, Petersen WA, Latham J, Ellis S, Christian HJ (2008) The relationship between lightning activity and ice fluxes in thunderstorms. J. Geophys. Res., 113:D15210. doi: 10.1029/2007JD009700

Dixon M, Wiener G (1993) TITAN: Thunderstorm identification, tracking, analysis, and nowcasting - A radar-based methodology. J. Atmos. Oceanic Technol., 10:785-797. doi: 10.1175/1520-0426(1993)010<0785:TTITAA>2.0.CO;2

Dolan B, Rutledge S (2009) A theory-based hydrometeor identification algorithm for X-band polarimetric radars. J. Atmos. Oceanic Technol., 26:2071–2088. doi: 10.1175/2009JTECHA1208.1

Dotzek N, Friedrich K (2009) Downburst-producing thunderstorms in southern Germany: Radar analysis and predictability. Atmos. Res., 93:457-473. doi: 10.1016/j.atmosres.2008.09.034

Evaristo R, Bals-Elsholz T, Williams E, Fenn AJ, Donovan M, Smalley D (2013) Relationship of graupel shape to differential reflectivity: theory and observations. Proc. 29th Conf. on Environmental Information Processing Technologies, Austin, USA, Amer. Meteor. Soc., 14. [Available online at https://ams.confex.com/ams/93Annual/webprogram/Paper214462.html.]

Foster TC, Hallett J (2002) The alignment of ice crystals in changing electric fields. Atmos. Res., 62:149-169. doi: 10.1016/S0169-8095(02)00008-X.

Greene DR, Clark RA (1972) Vertically integrated liquid water-A new analysis tool. Mon. Wea. Rev., 100:548-552. doi: 10.1175/1520-0493(1972)100<0548:VILWNA>2.3.CO;2

Hendry A, McCormick C (1976) Radar observations of the alignment of precipitation particles by electrostatic fields in thunderstorms, J. Geophys. Res., 81:5353–5357. doi: 10.1029/JC081i030p05353.

Jameson AR, Murphy MJ, Krider EP (1996) Multiple-parameter radar observations of isolated Florida thunderstorms during the onset of electrification. J. Appl. Meteor.., 35:343–354. doi: 10.1175/1520-0450(1996)035<0343:MPROOI>2.0.CO;2

Johnson JT, Mackeen PL, Witt A, Mitchell EDW, Stumpf GJ, Eilts MD, Thomas KW (1998) The storm cell identification and tracking algorithm: An enhanced WSR-88D algorithm. Wea. Forecasting, 13:263-276. doi: 10.1175/1520-0434(1998)013<0263:TSCIAT>2.0.CO;2

Kumjian MR, Ryzhkov AV (2008) Polarimetric signatures in supercell thunderstorms. J. Appl. Meteor.. Climatol., 47:1940-1961. doi: 10.1175/2007JAMC1874.1

Kumjian MR (2013) Principles and applications of dual-polarization weather radar. Part I: Description of the polarimetric radar variables. J. Oper. Meteor., 1:226-242. doi: 10.15191/nwajom.2013.0119

Lakshmanan V, Smith T (2010) An objective method of evaluating and devising storm-tracking algorithms. Wea. Forecasting, 25:701-709. doi: 10.1175/2009WAF2222330.1

Lund NR, MacGorman DR, Schuur TJ, Biggerstaff MI, Rust WD (2009) Relationships between lightning location and polarimetric radar signatures in a small mesoscale convective system. Mon. Wea. Rev., 137:4151–4170, 2009. doi: 10.1175/2009MWR2860.1

Machado LAT, and Coauthors (2014) The CHUVA Project – how does convection vary across Brazil? Bull. Amer. Meteor. Soc., 95:1–10. doi: 10.1175/BAMS-D-13-00084.1.

Matrosov SY, Reinking RF, Kropfli RA, Bartram BW (1996) Estimation of ice hydrometeor types and shapes from radar polarization measurements. J. Atmos. Oceanic Technol., 13:85–96. doi: 10.1175/1520-0426(1996)013<0085:EOIHTA>2.0.CO;2

Mattos EV, Machado LAT, Williams ER, Albrecht RI (2016a) Polarimetric radar characteristics of storm with and without lightning. Submitted to J. Geop.Res.

Mattos EV, Machado LAT, Williams ER (2016b) Thunderstorm Electrification and X-Band Polarimetric Radar: Thunderstorm Electrification Life Cycle. Submitted to J. Gep. Res.

Morel C, Orain F, Senesi S (1997) Automated detection and characterization of MCS using the meteosat infrared channel. Proc. Meteorological Satellite Data Users Conference, Brussels, 213-220.

Ryzhkov AV, Zrnic DS (2005) Radar polarimetry at S, C, and X bands: Comparative analysis and operational implications. Preprints, 32nd Conf. on Radar Meteorology, Albequerque, NM, Amer. Meteor. Soc., 9R.3. [Available online at http://ams.confex.com/ams/pdfpapers/95684.pdf.]

Ryzhkov A, Zrnic DS (2007) Depolarization in Ice Crystals and Its Effect on Radarimetric Measurements. J. Atmos. Oceanic Technol., 24:1256-1267. doi: 10.1175/JTECH2034.1

Ryzhkov AV, Kumjian MR, Ganson SM, Khain AP (2013a) Polarimetric radar characteristics of melting hail. Part I: Theoretical simulations using spectral microphysical modeling. J. Appl. Meteor. Climatol., 52:2849-2870. doi: 10.1175/JAMC-D-13-073.1

Ryzhkov AV, Kumjian MR, Ganson SM, Zhang P (2013b) Polarimetric radar characteristics of melting hail. Part II: Practical implications. J. Appl. Meteor. Climatol., 52:2871-2886. doi: 10.1175/JAMC-D-13-074.1

Sakuragi J, Biscaro T (2012) Determinação do viés do ZDR e seu impacto na classificação de hidrometeoros. XVII Congresso Brasileiro de Meteorologia, Gramado, Brazil, Sociedade Brasileira de Meteorologia, 1-5.

Schneebeli M, Sakuragi J, Biscaro T, Angelis CF, Costa IC, Morales C, Baldini L, Machado LAT (2012) Polarimetric X-band weather radar measurements in the tropics: radome and rain attenuation correction. Atmos. Meas. Tech., 5:2183-2199. doi: 10.5194/amt-5-2183-2012

Straka JM, Zrnic DS, Ryzhkov AV (2000) Bulk hydrometeor classification and quantification using polarimetric radar data: synthesis of relations. J. Appl. Meteor., 39:1341–1372. doi: 10.1175/1520-0450(2000)039<1341:BHCAQU>2.0.CO;2

Testud J, Le Bouar E, Obligis E, Ali-Mehenni M (2000) The rain profiling algorithm applied to polarimetric weather radar. J. Atmos. Oceanic Technol., 17:332-356. doi: 10.1175/1520-0426(2000)017<0332:TRPAAT>2.0.CO;2

Tuttle JD, Bringi VN, Orville HD, Kopp FJ (1989) Multiparameter radar study of a microburst: Comparison with model results. J. Atmos. Sci., 46:601-620. doi: 10.1175/1520-0469(1989)046<0601:MRSOAM>2.0.CO;2

Van Lier-Walqui, and Coauthors (2015) On polarimetric radar signatures of deep convection for model evaluation: columns of specific differential phase observed during MC3E. Mon. Wea. Rev. 144:737-758. doi: 10.1175/MWR-D-15-0100.1

Vila DA, Machado LAT, Laurent H, Velasco I (2008) Forecast and Tracking the Evolution of Cloud Clusters (ForTraCC) using satellite infrared imagery: Methodology and validation. Wea. Forecasting, 23:233-245. doi: 10.1175/2007WAF2006121.1

Vivekanandan JS, Ellis M, Oye R, Zrnic DS, Ryzhkov AV, Straka J (1999) Cloud microphysics retrieval using S-band dual-polarization radar measurements. Bull. Amer. Meteor. Soc., 80:381-388. doi: 10.1175/1520-0477(1999)080<0381:CMRUSB>2.0.CO;2

Weinheimer AJ, Few AA (1987) The electric field alignment of ice particles in thunderstorms, J. Geophys. Res., 92:14833–14844. doi: 10.1029/JD092iD12p14833.

Woodard CJ, Carey LD, Petersen WA, Roeder WP (2012) Operational utility of dual-polarization variables in lightning initiation forecasting. Electron. J. Oper. Meteor., 13:79-102. [Available online at http://www.nwas.org/ej/pdf/2012-EJ6.pdf.]

TABLE CAPTIONS

Table 1 Parameters definition and statistics for intense and non-intense events. For layer definition, see Section 4.1. Unities of trend parameters (# 2, 4, 6, 8, 10 and 13) are adimensional

Table 2 Modified contingency table with just hits and misses possible for each type of event

Table 1 Parameters definition and statistics for intense and non-intense events. For layer definition, see Section 4.1. Unities of trend parameters (# 2, 4, 6, 8, 10 and 13) are adimensional

#	Parameter	Layer	Parameter Threshold	Intense Events				Non-intense Events			Total		
				Maximum parameter average	Hits	Misses	POD	Hits	Misses	POD	Hits	Misses	POD
1	$dV(Z_h \geq 35)/dt$	MPL	+5 $km^3\ min^{-1}$	16.2 $km^3\ min^{-1}$	16	3	0.842	17	2	0.894	33	5	0.868
2	$V(Z_h \geq 35)/(V(layer))$	MPL	0.28	0.566	19	0	1.000	5	14	0.263	24	14	0.631
3	$dV(K_{DP} \geq 0)/dt$	MPL-1	+8 $km^3\ min^{-1}$	15.7 $km^3\ min^{-1}$	9	10	0.473	18	1	0.947	27	11	0.710
4	$V(K_{DP} \geq 0)/(V(layer))$	MPL-1	0.75	0.911	19	0	1.000	1	18	0.052	20	18	0.526
5	$dV(K_{DP} < 0)/dt$	MPL-2	+3 $km^3\ min^{-1}$	10.1 $km^3\ min^{-1}$	12	7	0.631	18	1	0.947	30	8	0.789
6	$V(K_{DP} < 0)/(V(layer))$	MPL-2	0.50	0.76	16	3	0.842	7	12	0.368	23	15	0.605
7	$dV(\rho_{hv} \leq 0.9)/dt$	MPL-1	+4 $km^3\ min^{-1}$	8.5 $km^3\ min^{-1}$	12	7	0.631	18	1	0.947	30	8	0.789
8	$V(\rho_{hv} \leq 0.9)/(V(layer))$	MPL-1	0.19	0.503	19	0	1.000	1	18	0.052	20	18	0.526
9	$dV(Z_{DR} < 0)/dt$	MPL	+11 $km^3\ min^{-1}$	29.6 $km^3\ min^{-1}$	13	6	0.684	16	3	0.842	29	9	0.763
10	$V(Z_{DR} < 0)/(V(layer))$	MPL	0.80	0.901	17	2	0.894	7	12	0.368	24	14	0.631
11	dH(40dBZ)/dt	40 dBZ top	15 $km\ h^{-1}$	23.9 $km\ h^{-1}$	14	5	0.736	10	9	0.526	24	14	0.631
12	VIL	Entire cell	16 $kg\ m^{-2}$	32.9 $kg\ m^{-2}$	17	2	0.894	18	1	0.947	35	3	0.921
13	d(VIL)/dt	Entire cell	0.02	2.9	12	7	0.631	17	2	0.894	29	9	0.763

Table 2 Modified contingency table with just hits and misses possible for each type of events

		Intense event	Non-intense event
Was intense event forecast? (i.e., Was threshold exceeded?)	Yes	Intense event hit	Non-intense event miss
	No	Intense event miss	Non-intense event hit

FIGURE CAPTIONS

Fig. 1 Sao Jose dos Campos CHUVA X-Band radar location (gray diamond), total radar coverage (100 km ray), study area (60 km ray), 19 intense events maximum reflectivity location (blue crosses), 10 independent intense events maximum reflectivity location (green triangles) and 19 non-intense events maximum reflectivity location (red X's)

Fig. 2 Maximum reflectivity temporal evolution for intense events (blue), independent intense events (black) and non-intense events (yellow). Time corresponds to the first time that a 35 dBZ rain cell was detected at 3 km CAPPI. For intense and independent events, only the event's time is plotted (when event reached 60 dBZ)

Fig. 3 Frequency of the maximum volume fraction and trend parameters values in terms of lead time. The black line presents the total for all parameters, divided by 10

Fig. 4 Average probability of nineteen intense events to become intense, according to the thirteen parameters, and its standard deviation. Zero minutes accumulated (yellow line and bars) means that only one lead time is computed, while six minutes accumulated (blue line and bars) means that the anterior time step is also computed. Twelve minutes considers the actual and the last two time steps (black line and bars)

Fig. 5 Average probability of ten independent events (blue line and bars) to become intense, according to the thirteen parameters, and its standard deviation. Individual independent event probabilities to become intense are plotted in yellow. For reference, the average probability of the nineteen intense events (black line and bars) to become intense is also plotted. All curves are accumulating twelve minutes in time

Fig. 6 Individual non-intense event probability to become intense (each yellow line), according to the thirteen parameters. The last non-intense events time steps are plotted on time equal to zero. For reference, the average probability of the nineteen intense events to become intense and its standard deviation are also plotted in black. All curves are accumulating twelve minutes in time

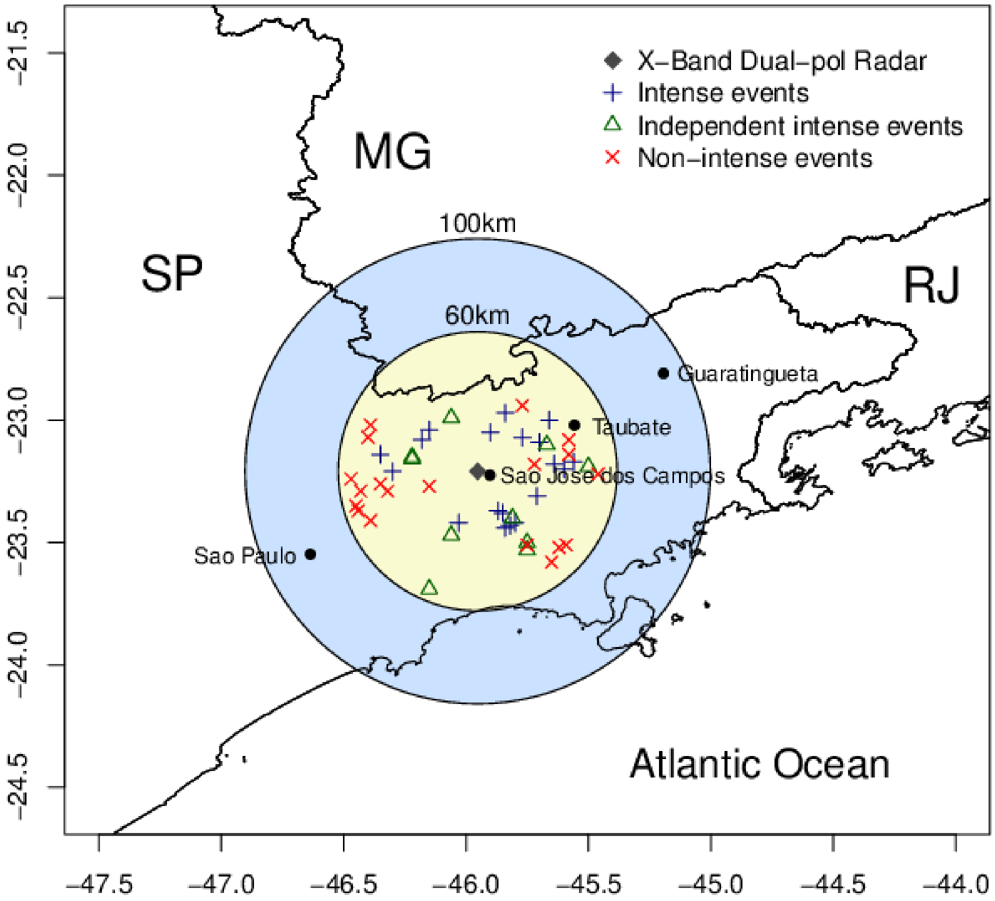

585

Fig. 1 Sao Jose dos Campos CHUVA X-Band radar location (gray diamond), total radar coverage (100 km ray), study area (60 km ray), 19 intense events maximum reflectivity location (blue crosses), 10 independent intense events maximum reflectivity location (green triangles) and 19 non-intense events maximum reflectivity location (red X's)

586

587

588

589

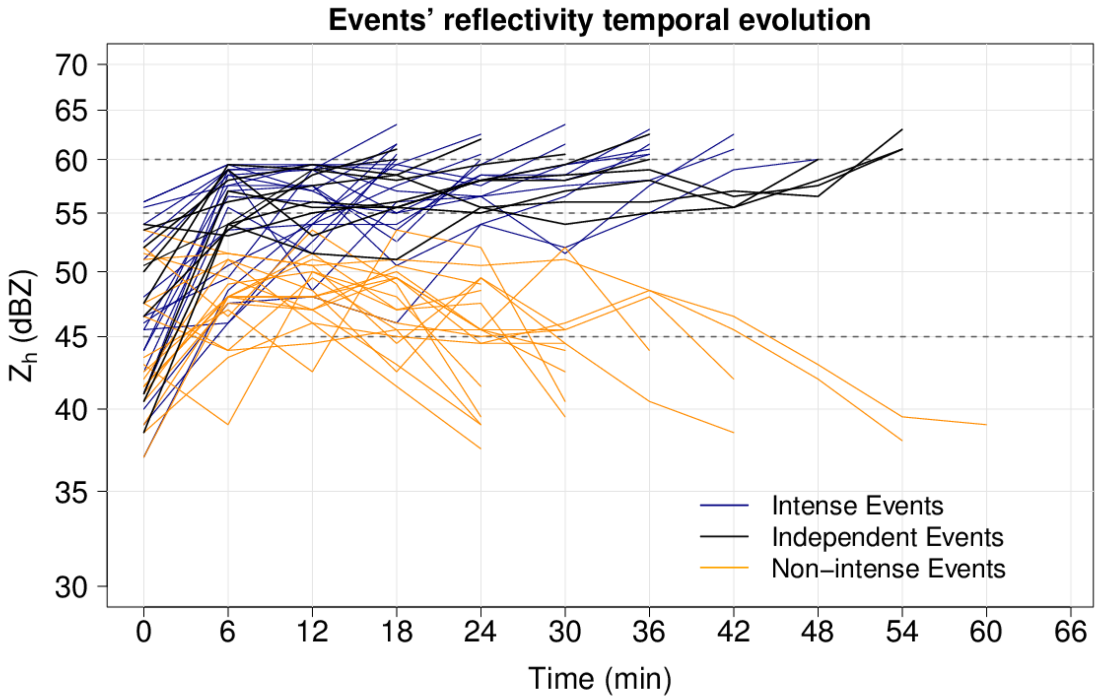

Fig. 2 Maximum reflectivity temporal evolution for intense events (blue), independent intense events (black) and non-intense events (yellow). Time corresponds to the first time that a 35 dBZ rain cell was detected at 3 km CAPPI. For intense and independent events, only the event's time is plotted (when event reached 60 dBZ)

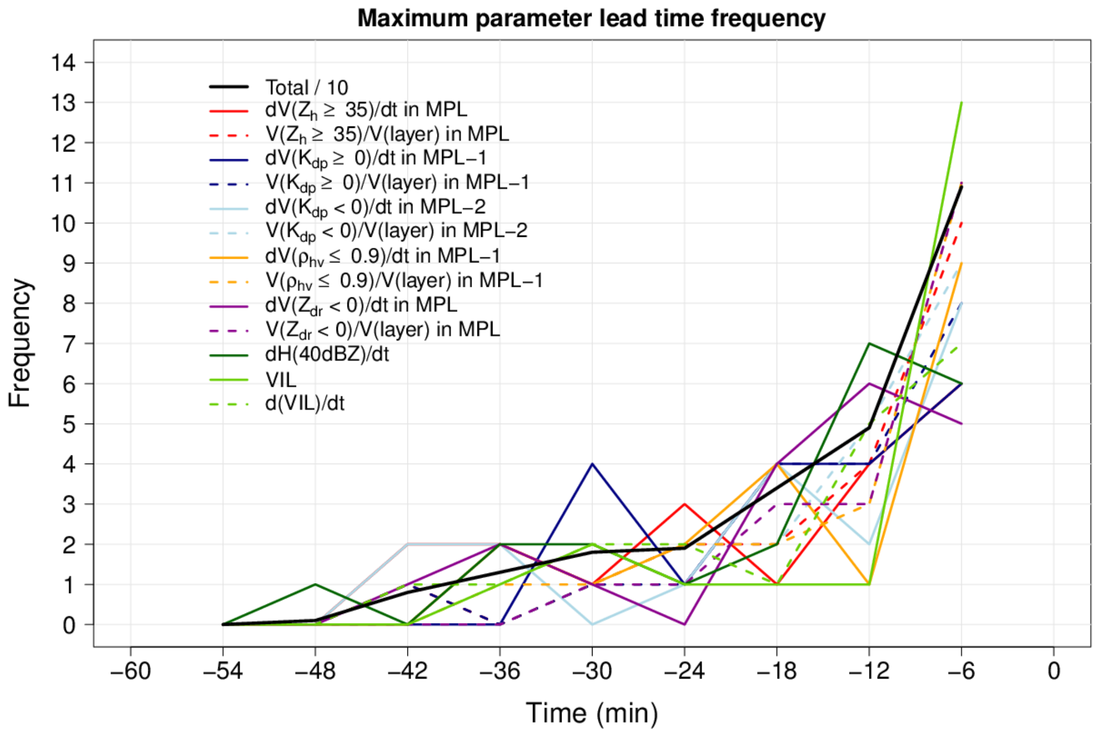

Fig. 3 Frequency of the maximum volume fraction and trend parameters values in terms of lead time. The black line presents the total for all parameters, divided by 10

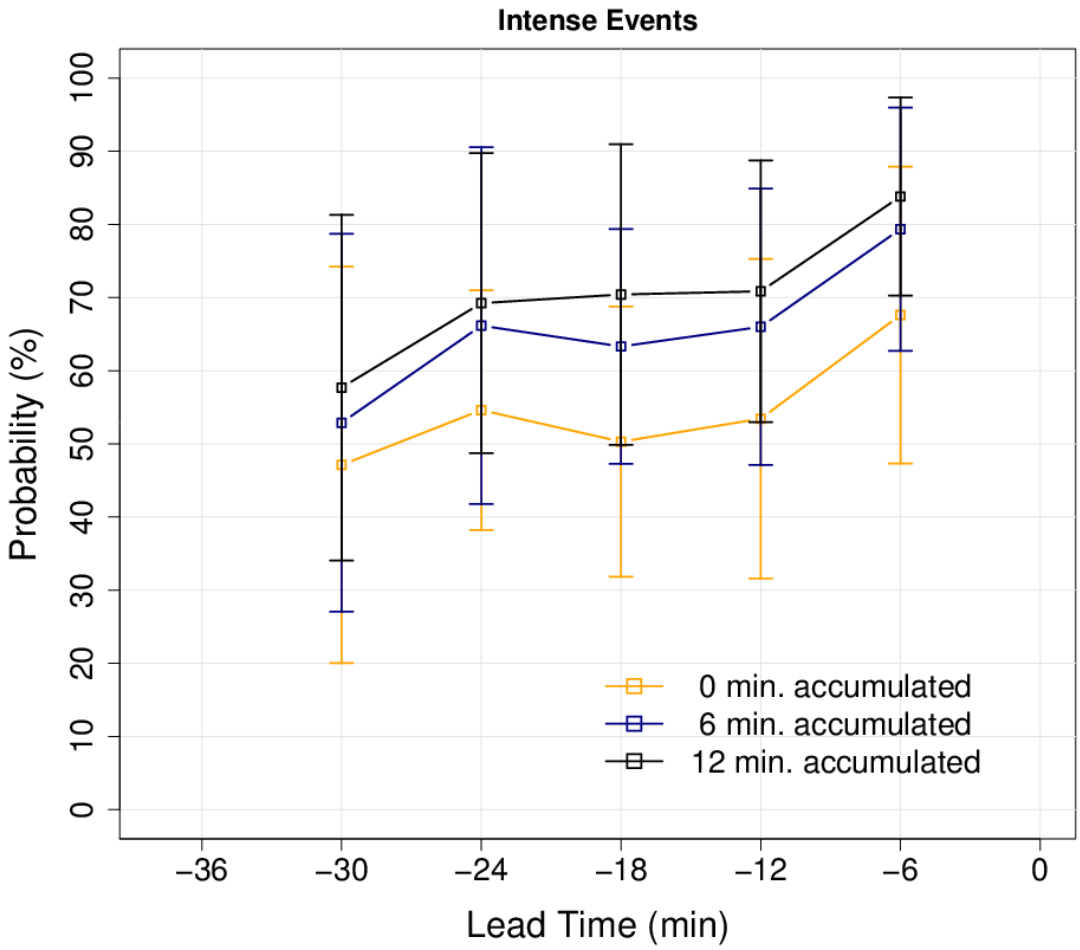

Fig. 4 Average probability of nineteen intense events to become intense, according to the thirteen parameters, and its standard deviation. Zero minutes accumulated (yellow line and bars) means that only one lead time is computed, while six minutes accumulated (blue line and bars) means that the anterior time step is also computed. Twelve minutes considers the actual and the last two time steps (black line and bars)

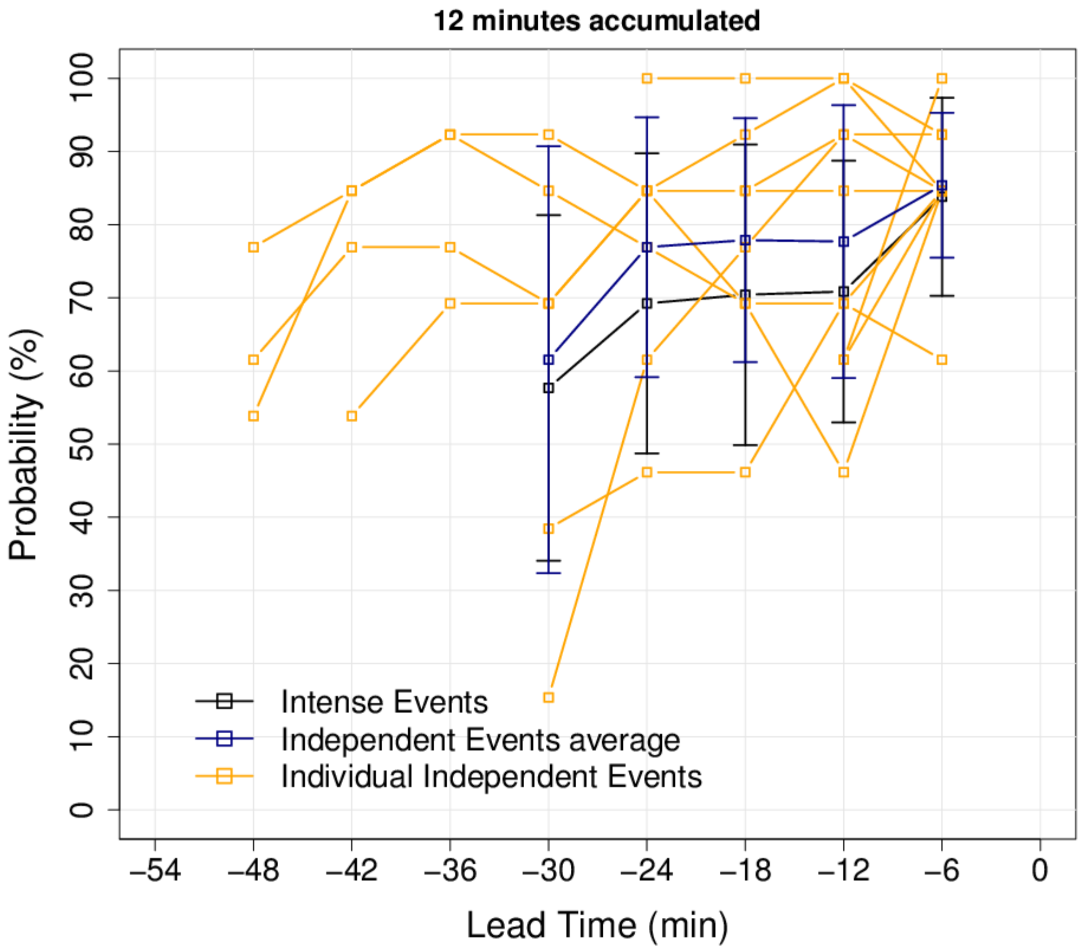

Fig. 5 Average probability of ten independent events (blue line and bars) to become intense, according to the thirteen parameters, and its standard deviation. Individual independent event probabilities to become intense are plotted in yellow. For reference, the average probability of the nineteen intense events (black line and bars) to become intense is also plotted. All curves are accumulating twelve minutes in time

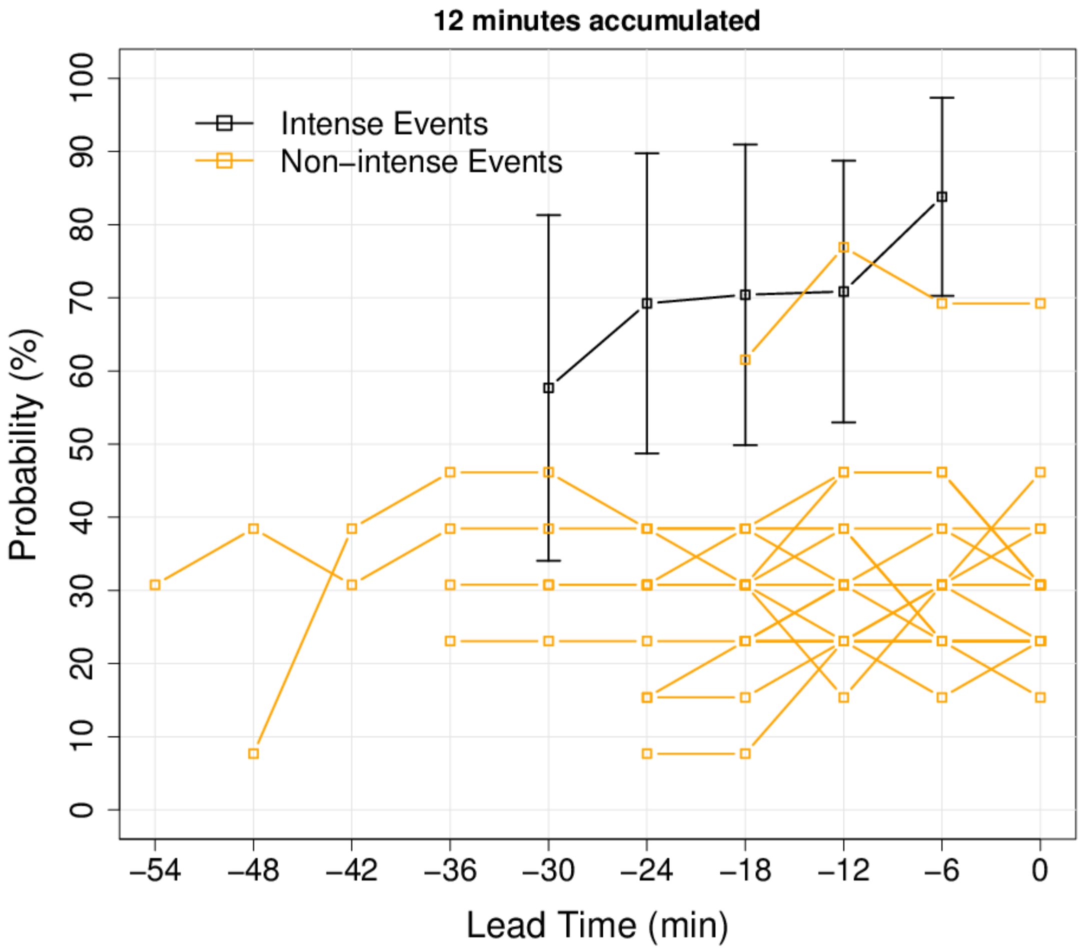

617

Fig. 6 Individual non-intense event probability to become intense (each yellow line), according to the thirteen parameters. The last non-intense events time steps are plotted on time equal to zero. For reference, the average probability of the nineteen intense events to become intense and its standard deviation are also plotted in black. All curves are accumulating twelve minutes in time